ECS Transactions, 69 (26) 27-40 (2015)
10.1149/06926.0027ecst ©The Electrochemical Society

Corrosion behavior of 13Cr casing steel in cement-synthetic pore solution exposed to high pressure CO_2 and H_2S

R. Feng[a,b], J. Beck[a], D. M. Hall[a,b], Aysel Buyuksagis[a], M. Ziomek-Moroz[d,*], S. N. Lvov[a,b,c,†]

[a] The EMS Energy Institute, Pennsylvania State University, University Park, PA 16802, USA
[b] Department of Energy and Mineral Engineering, Pennsylvania State University, University Park, PA 16802, USA
[c] Department of Materials Science and Engineering, Pennsylvania State University, University Park, PA 16802, USA
[d] National Energy Technology Laboratory, U.S. Department of Energy, 1450 Queen Avenue SW, Albany, OR 97321, USA

The electrochemical corrosion behavior of grade L-80, type 13Cr casing steel was investigated in cement-synthetic pore solution (CSPS) exposed to CO_2 and H_2S using in-situ electrochemical methods and ex-situ surface analyses at 85 and 200 °C, respectively. Total system pressure was 10 MPa. Corrosion rates increased significantly when the temperature increased from 85 to 200 °C. Limiting current behavior was observed for the anode reaction, while charge-transfer control was observed for the cathode reaction. Surface analyses revealed the presence of $CaCO_3$ on the surface at both temperatures and $FeCO_3$-like deposits at 200 °C.

1. Introduction

As deeper wells are drilled for oil and gas extraction, the exploration and production tubulars encounter higher pressures, temperatures, and concentrations of corrosive species in the downhole environment. Thus, it becomes increasingly important to consider the integrity of the casing steel that provides both support and isolation of the well during the production. (1-3) These casings are commonly cemented to provide better sealing, and the alkaline environment provided by the pore water at the cement-casing interface typically puts the steel in a passive region. (4-5) However, exposure to acid gases such as CO_2 and H_2S can cause degradation of the cement and thus lower the pH at the cement-steel interface. (6-8) Furthermore, many formation waters are brines containing high concentrations of chlorides, which could penetrate the cement and cause depassivation or passive film breakdown on the casing steel surfaces. (9,10) These factors increase the risk of corrosion and failure of the well casing. Also, literature data indicate that steels are more susceptible to sulfide stress corrosion cracking with the presence of H_2S for both carbon steels and 13Cr-martensitic stainless steels. (11-13)

* Corresponding author: Tel: (541) 967-5943; fax: (541) 967-5880. Margaret.Ziomek-Moroz@NETL.DOE.GOV.
† Corresponding author: Tel.: (814) 863-8377; fax: (814) 865-3248. E-mail address: lvov@psu.edu.

In previous tests, the cement pore solution composition was determined after exposure of Class H cement to acid gas CO_2 and formation brines, and the corrosion of casing steel L-80 was investigated in the cement synthetic pore solution (CSPS) in contact with 10 MPa CO_2. (14) Therefore, in this work, the corrosion behavior of casting steel L-80 was further investigated in the CSPS in contact with a CO_2 and H_2S mixture at 85 °C and 200 °C, respectively. In-situ electrochemical measurements, ex-situ surface analyses, and mass loss sample measurements were performed to study of H_2S and temperature effects.

2. Experimental

2.1. Materials and Preparation

The steel investigated in this study was grade L-80, type 13Cr, which is commonly used as casing steel by the oil and natural gas industry. The chemical composition of L-80 is listed in TABLE I. (15) This grade has been approved for sour environments under ANSI/NACE MR0175/ISO 15156. (15) Use of higher-alloyed casing materials, particularly 13Cr alloys, has reportedly increased in recent years as operators have started to plan for possible extensions of well life beyond original designs. (16)

TABLE I. Chemical composition (max, %wt.) of L-80. (15)

Grade	Fe	C	Cr	Ni	P	S	Mn	Cu
L-80	Bal	0.15-0.22	12-14	0.5	0.2	0.1	0.25-1	0.25

The steel was machined to plate samples with the dimensions of 10×10×5 mm. The plate samples were coated with an epoxy over all the surfaces except for one of the 10×10 mm faces, which was exposed to the test solutions and faced the counter electrode. The exposed surface was wet ground with 600 grit SiC paper. The steel electrode was cleaned with propanol and distilled water and then wiped dry with lint-free wipes. The wire attached to the steel samples were coated with shrinkable polytetrafluoroethylene (PTFE) tubing to protect the leads and avoid a short circuit with the autoclave vessel.

2.2. System Setup

The electrochemical measurements were performed using a typical three-electrode system in the autoclave vessel. The working electrode was the prepared steel samples, and the counter electrode was a platinum plate or mesh with the dimensions of 10×20×1 mm, which was coated with epoxy similarly to working electrodes. All the wires attached to the electrodes were covered with PTFE shrinkable tubing. Three working electrodes were sealed into a PTFE plate using epoxy such that all three polished faces were exposed on a flush surface. A counter electrode was placed through a hole in the PTFE plate near each working electrode, and the leads were bent at a right angle to provide a parallel surface with respect to the working electrodes.

A double-junction Ag/AgCl electrode was used as the reference electrode to minimize the contamination from the corrosive test solutions. The fill solution for the

outer junction was 5 %wt. NaCl(aq) solution to minimize the junction potential difference from the concentration gradient between the reference electrode and the test solutions. The inner junction was prepared by sealing the Ag/AgCl at one end of an alumina tube and filling the tube with a reference solution-zirconia sand mixture. The purpose of the sand was to provide a diffusion barrier and extend the life of the electrode. The inner junction was closed with a porous zirconia-magnesia cement. The outer junction was formed by sealing a PTFE tube to the outside of the alumina tube. This junction was again filled with a reference solution-zirconia sand mixture and close with porous zirconia-magnesia cement. The potentials versus the standard hydrogen electrode (SHE) were calculated using data from HCh thermodynamic software to be 0.193 and 0.076 V at 85 and 200 °C, respectively. (17) The values were confirmed by comparing against thermodynamic properties and activity coefficients found in literature. (18)

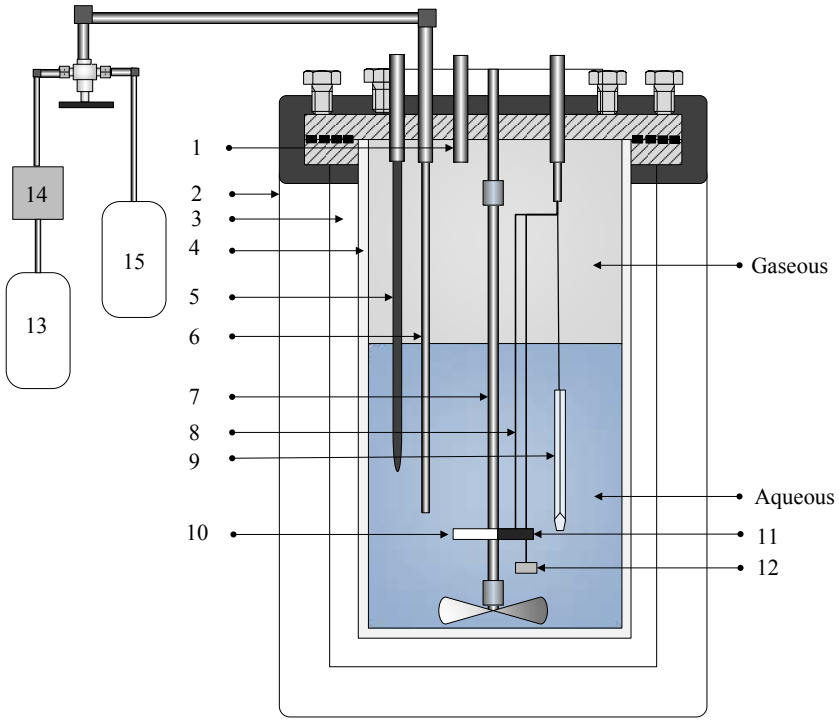

Figure 1. Schematic of the autoclave system.
1- Connection to pressure transducer; 2- Heating mantle; 3- Autoclave stainless steel vessel; 4- PTFE liner; 5- polymer-coated thermocouple; 6- dip tubing; 7- Epoxy-coated stirrer; 8- PTFE-coated lead; 9- Ag/AgCl reference electrode; 10- PTFE assembly; 11- working electrode; 12- Pt counter electrode; 13- CO_2 cylinder; 14- supercritical CO_2 pump; 15- H_2S/N_2 cylinder.

The autoclave was a Parr 4560 system, which consisted of a 450 mL stainless steel reactor vessel, a PTFE liner which was used to contain the corrosive test solution, and the autoclave lid. The available volume of the autoclave was 360 mL when assembled. Mounted in the lid were a thermocouple, a pressure transducer, and a steel dip tube for the injections of gas and solutions. The thermocouple was inserted into a 316 stainless steel thermowell so that the sensor could be protected from corrosion. Working with the thermocouple, a heating mantle around the vessel was used to control the temperature. The stainless steel stir rod inside the vessel was coated with epoxy to prevent undesired

corrosion. PTFE compression glands were used to seal the wires coming out from the vessel. A schematic diagram of the autoclave is shown in Figure 1.

2.3. Test Solutions and Experimental Procedure

The test solution was designed to simulate the pore water present at the cement-casing interface in the presence of CO_2 and H_2S over a temperature range from 85 to 200 °C. The simulated pore water was based on a previous study on cement-casing corrosion in a supercritical CO_2 environment, and the composition is presented in TABLE 2. (11) It has been reported in literature that in deep wells the ratio of CO_2:H_2S can be expected to be on the order of 1000, and this ratio was selected for the tests reported here. (14) A mole ratio of 0.05 for CO_2:H_2O was selected, as this allowed an adequate volume of solution to ensure coverage of the electrodes and weight loss samples at both 85 and 200 °C. The solution pH was calculated using OLI Analyzer software taking account of temperature, system volume, and solution composition. The pH values are also given in TABLE 2.

TABLE 2. Solution composition (mol kg^{-1} H_2O) and pH for assembled systems.

KCl	NaCl	Na_2SO_4	$CaCl_2$	$Ca(OH)_2$	CO_2	H_2S	N_2	pH, 85 °C	pH, 200 °C
0.0395	0.0476	0.125	0.00557	0.190	2.78	0.00278	0.025	5.28	5.93

The solution was prepared with 243 g of deionized water at 85 °C and 171 g at 200 °C. These values were calculated using OLI Analyzer software to provide the desired test conditions at each temperature while ensuring that the autoclave would be at least halfway filled with solution. The autoclaves were assembled dry with the electrodes and weight loss samples. The desired amount of each salt from TABLE 2 was added to the bottom of the vessel before it was sealed. After sealing, the vessel was deaerated by purging with CO_2 and brought back to just above ambient pressure. Next a gas mixture of 10%vol. H_2S in N_2 was added to the vessel to dose with the required amount of H_2S. Deionized water was deaerated with argon for at least 1 hour before a high pressure diaphragm pump was used to inject at a rate of 10 mL min^{-1} to provide the desired amount of water. The system was pressurized to 700 psi with CO_2 and then brought to the test temperature. Once the final temperature was reached, a supercritical CO_2 pump was used to pump in more CO_2 and bring the total system pressure up to 10 MPa. At this point the corrosion measurements were started.

Electrochemical measurements were performed using a computer-controlled Gamry Reference 600 and PCI450 potentiostats. The in-situ electrochemical measurements included linear polarization resistance (LPR), electrochemical impedance spectroscopy (EIS), cyclic voltammetry (CV), and linear sweep voltammeter (LSV) for Tafel slope analysis. The autoclave was stirred at 140 RPM. LPR was carried out over the potential range of ±10 mV with respect to the corrosion potential (E_{corr}) equal to the open-circuit potential (E_{opc}) after 60 hour-sample exposure, and the scan rate was 0.1 mV s^{-1}. EIS was measured over the frequency range of 300 kHz to 5 mHz with the amplitude of 10 mV. After 60 hours of sample exposure, CV was performed at scan rates of 100, 50, and 10 mV s^{-1} from -500 mV to +750 mV vs $E_{corr.}$ LSV was carried out at a scan rate of 1 mV s^{-1}. After the corrosion tests, the corroded surfaces were investigated using scanning electron microscopy (SEM) with energy dispersive X-ray spectroscopy (EDS). The mass loss

samples were cleaned and weighed according to ASTM G1-03 using Solution C.3.5 (HCl and hexamethylene tetramine) from Appendix A1. (20)

2.4. Calculation of Corrosion Rate

In a three-electrode cell, when corrosion was under activation control and a small polarization was applied, the corrosion current density, $j_{corr,}$ can be calculated according to Stern-Geary equation, shown in Equations [1] and [2]. (21,22)

$$1/ R_{pol} = j_{corr} B' \quad [1]$$

$$B' = (\ln 10) (b_c + b_a) / (b_c b_a) \quad [2]$$

where R_{pol} is the area-specific linear polarization resistance and B' is a simple combination of the cathodic, b_c, and anodic, b_a, Tafel slopes. R_{pol} was measured from LPR and corrected for the area-specific solution resistance (R_{sol}) obtained from EIS. The Tafel slopes were calculated according to Equation [3] assuming the anodic and cathodic symmetry coefficients, β_a and β_c, to be 0.5.

$$b_c = b_a = \ln 10 \ (RT)/(\beta_c nF) = \ln 10 \ (RT)/(\beta_a nF) \quad [3]$$

where R is the ideal gas constant, T the absolute temperature, n the electron number being transferred, and F the Faraday constant.

The corrosion rate, defined as the depth of corrosion penetration per time, can be calculated following Equation [4].

$$\text{Corrosion rate (CR)} = j_{corr} M / (nF\rho) \quad [4]$$

where M is the molecular mass of the corroding metal and ρ is the metal density.

3. Results and Discussion

3.1. Primary Species

The dominant species in the aqueous phase at each temperature were predicted using OLI Analyzer thermodynamic modeling software. In both cases the majority of Ca (>95%) was predicted to precipitate as either calcium carbonate or calcium sulfate. Due to the low solubility of calcium hydroxide and the reaction between $Ca(OH)_2$ and CO_2, the pH was predicted to be directly dependent on the ratio of $Ca(OH)_2$:CO_2 in the system. For a ratio above 1, only some of the $Ca(OH)_2$ turned into $CaCO_3$ through carbonation, and the solution would be readily saturated with calcium hydroxide and the pH would hold steady around 10.95 at 85 °C and 9.67 at 200 °C. As the ratio approaches 1, the calcium is totally converted to calcium carbonate and the pH begins to drop. Once the ratio drops below 1, the pH becomes dependent on the solubility and dissociation of carbonic acid and the subsequent reactions with other species, and an acidic environment is created. The tested conditions contained a $Ca(OH)_2$:CO_2 ratio well below 1, resulting in a weakly acidic environment of 5.28 and 5.93 at 85 and 200 °C, respectively. The low

solubility and high content of $Ca(OH)_2$ in Portlandite cement provides a considerable buffering capacity to maintain high pH; however, once the calcium is converted to calcium carbonate the buffering is minimal.

Due to the lower pH, the dominant form of sulfide was predicted to be undissociated $H_2S(aq)$. Interestingly, the model predicted roughly equal distribution of H_2S between the predominantly aqueous and CO_2 phases. Much like CO_2, the dominant effect of H_2S on the pore solution is expected to be the neutralization of $Ca(OH)_2$. Thus, unless the ratio of $Ca(OH)_2$:H_2S approaches 1, the presence of H_2S is expected to have a minimal impact on the solution pH.

3.2. Corrosion Rates

The corrosion rates for the L-80 material (referred from here on as Electrodes) calculated from the LPR and EIS results and measured from mass loss samples are listed in TABLE 3. The averages and standard deviations were calculated using three sequential data points after 60 hours of exposure. While general agreement was seen between the LPR and EIS results for each sample at 85 °C, it can be seen that there was significant variation in corrosion rate between the samples. While the corrosion rate from Electrode 1 agreed with Sample 2 for mass loss, Sample 1 gave a higher corrosion rate by a factor of 10 while Electrodes 2 and 3 were lower by about a factor of 3 to 5. By comparison, measurements for the same alloy in the same solution but at 100 °C and 10 MPa of CO_2 found corrosion rates that ranged between 0.02 and 0.14 mm y^{-1}. (11) This would suggest that the presence of H_2S slowed the overall corrosion rate by up to as much as a factor of 10.

TABLE 3. The corrosion rates (mm y^{-1}) from LPR, EIS and mass loss samples.

Temperature		**LPR**	**EIS**	**Mass Loss**
85 °C	Sample 1	0.0210±*0.0046*	0.0281±*0.0068*	0.372±*0.006*
	Sample 2	0.00492±*0.00152*	0.00274±*0.00007*	0.0337±*0.0167*
	Sample 3	0.00738±*0.00381*	0.00782±*0.00293*	-
200 °C	Sample 1	1.61±*0.01*	0.529±*0.060*	0.0724±*0.0335*
	Sample 2	0.506±*0.020*	-	0.0747±*0.0320*
	Sample 3	1.55±*0.09*	-	-

The electrochemical results had a much stronger agreement with each other at 200 °C, and the corrosion rate was seen to increase by two orders of magnitude. This was similar to results observed by the authors for high strength drill pipe steel in alkaline solutions with H_2S where an increase in temperature from 85 to 200 °C resulted in an increase of corrosion rate by a factor of 10. (23) However, the mass loss samples had a corrosion rate much lower than the electrochemical measurements, and were on a similar order to the results at 85 °C. It is currently undetermined what caused the drastic variation between the various samples. As all samples at a single temperature were present in the same autoclave vessel at the same time, they were exposed to the same environment. Thus, any differences affecting the corrosion rates must have derived from the respective samples surfaces. One possibility is that unwanted differences in surface preparation had an

unexpected yet dramatic effect on the resulting corrosion rate values Another possibility is that calcium carbonate precipitation resulted in uneven scaling on the sample surfaces, and thus affecting the corrosion rate values.

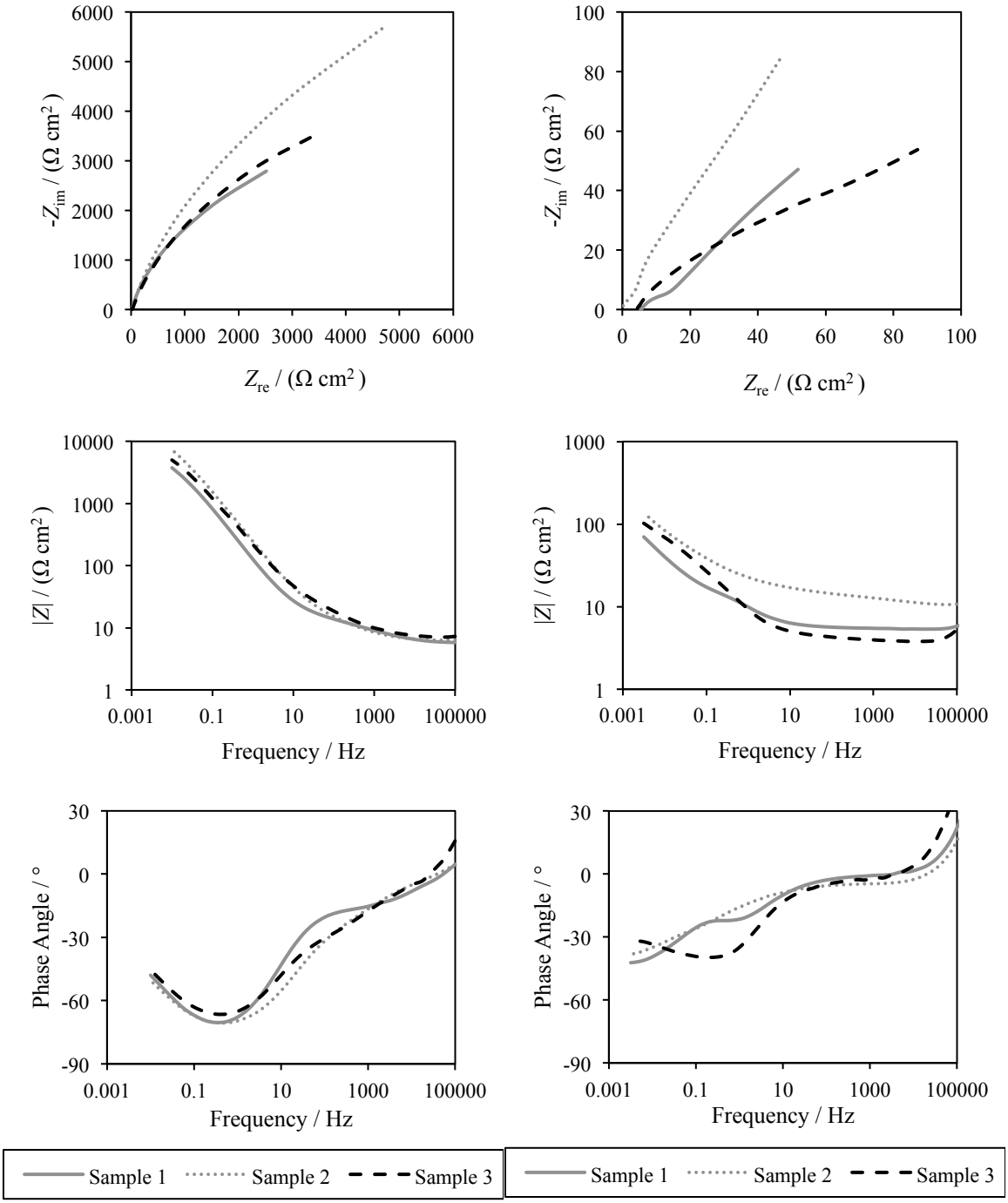

Figure 2. The EIS results of L-80 electrodes corroded in CSPS at 85 °C (left) and 200 °C (right).

3.3. EIS Results

The EIS results of L-80 electrodes corroded in CSPS at 85 and 200 °C are given in Figure 2. At 85 °C two well-defined time constants can be seen in the phase angle plots, which were fit using the equivalent circuit shown in Figure 3. Results from the fitting are given in TABLE 4. The low frequency phase angle peak extended well beyond -45 °, suggesting that Warburg diffusion from the bulk solution did not have any observable effect on the corrosion behavior. This was further confirmed by performing measurements at unstirred conditions, where the impedance curves were found to overlap almost perfectly with the stirred measurements. It appears that the low frequency time constant correlated with the passive film on the sample surface.

As with the LPR results, it can be seen that the total impedance dropped by about 100 times when the temperature was increased to 200 °C. Electrode 1 showed a similar two-time constant behavior as the tests at 85 °C. However, the impedance results for Electrodes 2 and 3 were less consistent and could not be readily fit by any of the common equivalent circuits. Results under unstirred conditions did not change from the stirred case, suggesting again that diffusion from the bulk solution was not affecting the corrosion process. An investigation is currently underway to determine any impedance models that could explain the observed behavior, as well as to explain why three samples in the same solution could display such differing behaviors.

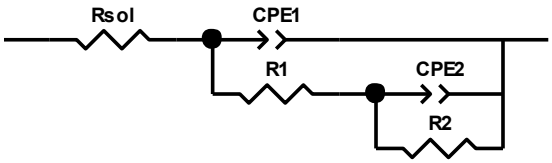

Figure 3. The equivalent circuit used to fit the EIS results.

TABLE 4. The fitting results of EIS results using the equivalent circuit in Figure 3.

T / °C	Sample	R_{sol} / Ω cm^2	$R1$ / Ω cm^2	$R2$ / Ω cm^2
85	1	5.99±0.13	13.3±1.3	5,669±255
	2	6.81±0.08	23.6±4.1	65,569±3582
	3	7.76±0.20	37.2±12	18,042±3,785
200	1	4.53±0.01	10.0±0.4	465±46

3.4. CV Results

The CV results of L-80 at 85 and 200 °C at 100, 50, and 10 mV s^{-1} are given in Figures 4 and 5, respectively. At 85 °C an obvious limiting current effect was observed in the anodic region, as well as a set of redox peaks between 0 and 0.1 V vs. SHE. The E_{corr} was -0.353±0.014 for the samples, meaning that these peaks occurred at polarizations well beyond where the corrosion was occurring. These peaks were not observed for L80 in the same CSPS at 100 °C and 10 MPa CO_2, meaning that the redox reaction likely corresponded to a sulfide-containing reaction. (11)

The limiting current around E_{corr} appears to be due to passivation from the high chromium content of the steel. Effects due to capacitive charging were apparent, as the current magnitude steadily decreased with decreasing scan rate. At 10 mV s^{-1}, it was observed that the backward scan in the anode region had a higher current than the forward scan. Also, a hysteresis was observed, which can be correlated to pitting susceptibility of the L-80 material. (24)

The behavior at 200 °C was considerably different. The redox couple at large anodic polarization was not readily observed, and the effect of scan rate on the current magnitude was much more pronounced. A limiting current on anodic polarization was still present, though it was only observed at 10 mV s^{-1}. The sweeps at 50 and 10 mV s^{-1} could not be extended beyond 0 V vs. SHE, as it resulted in excessive noise during the cathodic sweep. Low levels of this noise can be seen between -0.5 and -0.75 V vs. SHE for the 100 mV s^{-1} sweep.

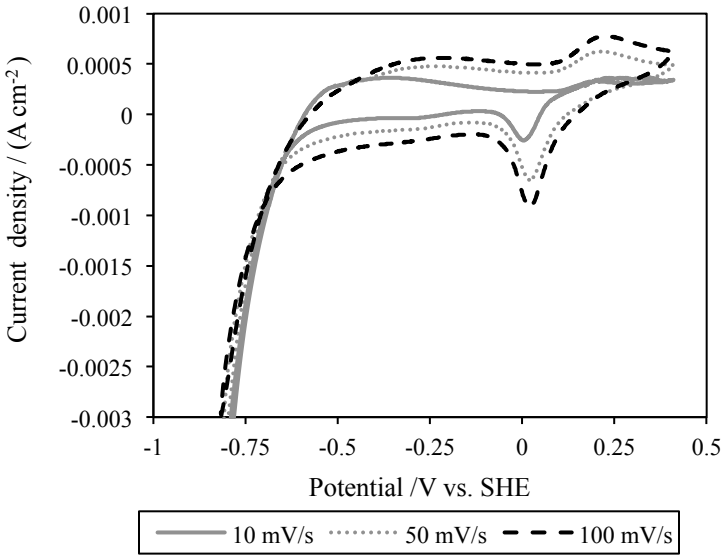

Figure 4. The CV plots of L-80 at 85 °C at the sweep rate of 10, 50, 100 mV s^{-1}.

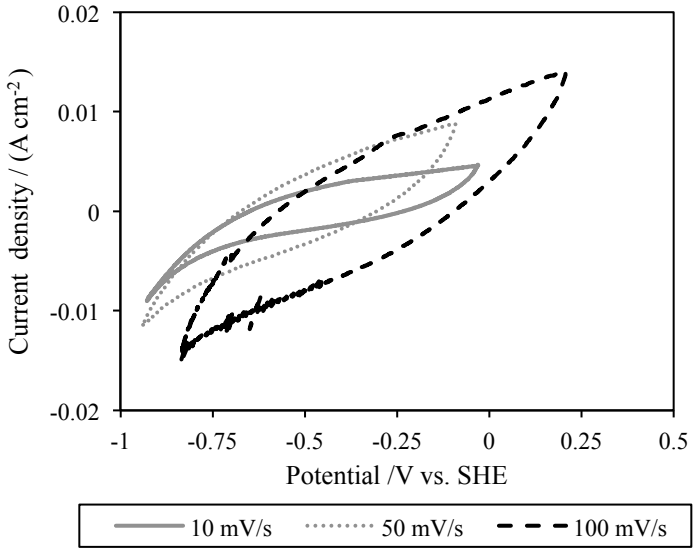

Figure 5. The CV plots of L-80 at 200 °C at the sweep rate of 10, 50, 100 mV s^{-1}.

3.5. LSV Results and Tafel Analysis

The LSV plots of Sample 3 at 85 °C and Sample 2 at 200 °C are given in Figure 6. The Tafel analysis results for all the samples are listed in TABLE 5. As mentioned earlier, the sweeps were performed in each direction starting at the measured E_{corr}. However, at 85 °C it can be seen that E_{corr} shifted in the negative direction after the anodic polarization. This shift was not seen at 200 °C, suggesting that the surface at 85 °C was much more sensitive to polarization effects. Generally, the current density was higher at 200 °C than at 85 °C, confirming again that the corrosion rate was faster at higher temperature.

For the anodic region, a limiting current was observed at 85 °C, and a slightly inclined slope at 200 °C, indicating that the anodic reactions were limited at 85 °C and depressed at 200 °C. This behavior was also observed in the CV curves at 10 mV s^{-1}. It was expected that this limitation was due to passivation from the formation of a chromate-rich layer. While the effect was still observed to some extent at 200 °C, it is believed that the elevated temperature either led to an increased rate of dissolution of the passive film or a higher prevalence of defects.

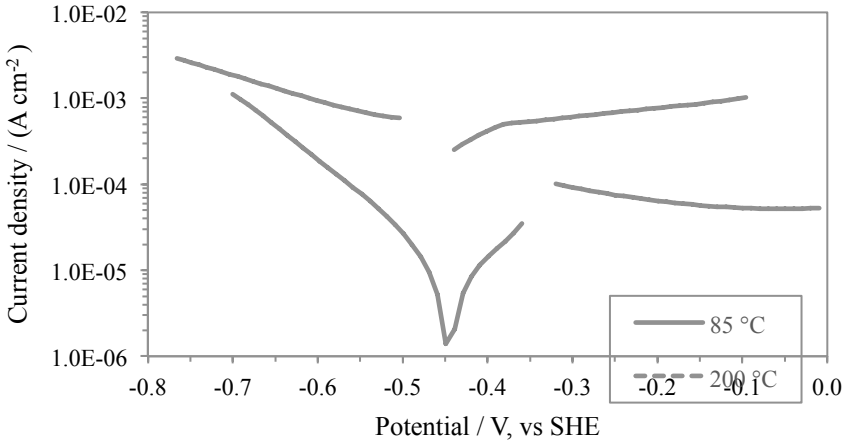

Figure 6. The LSV plots of Sample 3 at 85 °C and Sample 2 at 200 °C with the sweep rate of 1 mV s^{-1}.

TABLE 5. The Tafel analysis results.

V dec^{-1}	85 °C	200 °C
b_a	limiting	>1
b_c	0.131±0.011	0.308±0.044
b_c-VH	0.142	0.188

For cathodic polarization, linear regions were observed. One commonly accepted mechanism for hydrogen evolution reaction (HER) is the Volmer-Heyrovsky (VH) mechanism. (24) The cathodic slopes of VH mechanism were calculated according to $\ln 10RT/(\beta_c F)$ and are listed in TABLE 5 for comparison. The cathodic slope (b_c) at 85 °C indicated the VH mechanism, whereas b_c at 200 °C was much larger and might be related to a different mechanism. At both temperatures no limiting current effects were observed over the potential regions swept.

3.6. Corrosion Products

The corroded surfaces after the tests at 85 and 200 °C were analyzed with SEM and EDS, and the SEM images are shown in Figures 7 and 8, respectively. EDS spot analyses were performed at representative spots on the surfaces which are marked in the images, and the results are listed in TABLE 6.

At 85 °C, the steel surface was covered with a very thin light white color film noted through visual observation. The SEM results showed that the thin film consisted of small crystalline particles with a size of 1 – 5 μm on the surface. EDS results showed that the crystalline structure has a chemical composition similar to $CaCO_3$(s), like Location 1 in Figure 7. In some areas, almost the steel bare surface was exposed, like Location 3 in Figure 7. The result here is from Electrode 3, where the measured corrosion rate was notably lower than from Electrode 1 or either of the two weight loss samples. Uneven scaling of $CaCO_3$ between all of the test samples at 85 °C may help explain the discrepancy between the measured corrosion rates.

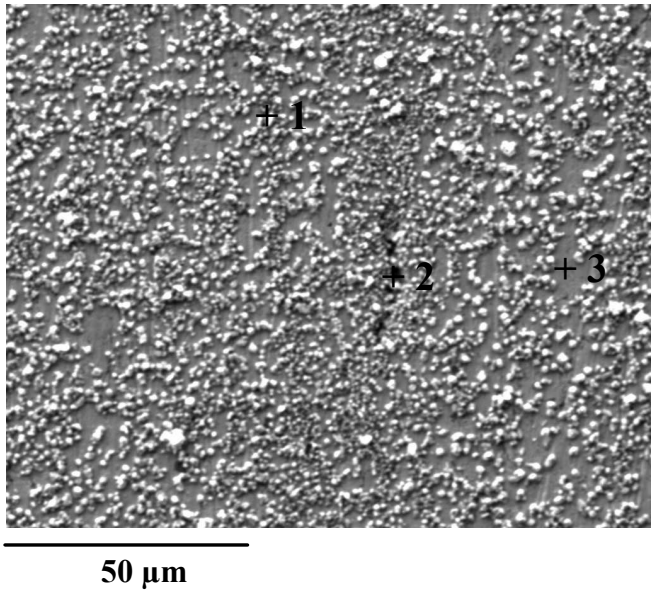

Figure 7. The SEM image of L-80 corroded in CSPS at 85 °C.

At 200 °C, the steel surface was covered with a black film. The SEM results showed that the film was very non-uniform. The sizes of particles on the surface were larger (5 - 10 μm). EDS results showed that the chemical composition was very close to a mixture of $FeCO_3$(s) and $CaCO_3$(s). The higher amount of $FeCO_3$(s)-like scales at 200 °C were probably due to the faster corrosion rate, like Location 3 in Figure 8.

At both 85 and 200 °C it was noted that the chromium content was very low at most regions. This suggested that the chromate film was either too thin to be observed at the accelerating voltages used or was poorly formed in the test environments. Sulfur content on the surface was also typically quite low. While this may mean that the formation of iron sulfide products were not preferred in the test environment, previous experience of the authors with similar H_2S-containing corrosion systems suggests that any formed sulfides may have been unstable and readily degraded into iron oxide and H_2S on exposure to air and rinse water. The low pH may also have increased the solubility of iron sulfide.

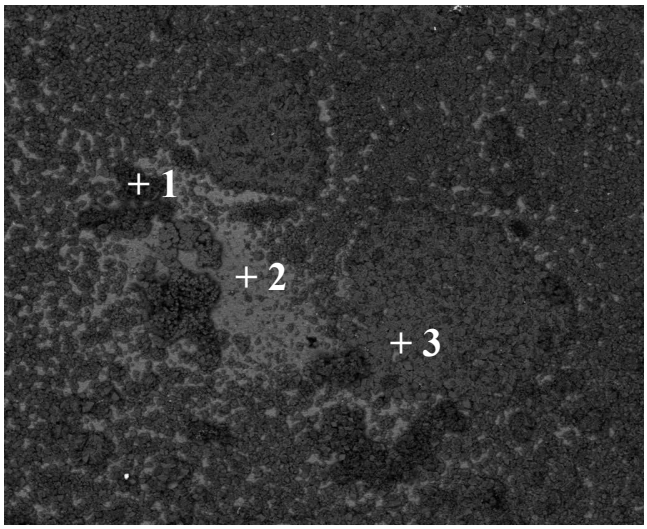

Figure 8. The SEM image of L-80 corroded in CSPS at 200 °C.

TABLE 6. EDS chemical analyses (%at.) on the corroded L-80 surfaces in selected locations marked in Figures 7 and 8.

No.	Location	Fe	C	O	S	Ca	Cr
85 °C	1	2.64	18.16	60.03	0.97	17.19	-
	2	10.21	28.41	49.27	0.74	9.93	-
	3	74.58	5.63	-	-	-	19.31
200 °C	1	1.9	18.57	59.57	0.2	18.7	-
	2	9.62	25.08	50.49	0.3	0.08	5.97
	3	17.26	19.86	58.71	0.05	4.13	-

4. Conclusions

Corrosion testing was performed for a casing steel grade L-80, type 13Cr in a simulated cement pore solution exposed to CO_2 and H_2S at 10 MPa. Thermodynamic modeling predicted that all calcium hydroxide would be converted to calcium carbonate at the conditions tested, resulting in a weakly acidic solution. Electrochemical tests showed a considerable increase in corrosion rate from 85 °C to 200 °C. Mass loss results were inconsistent and did not always agree with electrochemical tests. EIS generally showed two time constants, and the impedance at 200 °C was smaller than at 85 °C. The cathodic

region was found to be charge-transfer controlled, while anode regions showed limiting current behavior at both temperatures. The cathodic slopes at 85 °C matched what was predicted assuming the Volmer-Heyrovsky mechanism for hydrogen evolution. Cyclic voltammetry showed obvious anodic current peaks for 85 °C that were not present at 200 °C. Surface analysis found considerable $CaCO_3$-like phase at both temperatures and more $FeCO_3$-like phase at 200 °C, confirming the higher corrosion rate at higher temperature and suggesting that scaling may have had a significant effect on the corrosion behavior.

Disclaimer

This report was prepared as an account of work sponsored by an agency of the United States Government. Neither the United States Government nor any agency thereof, nor any of their employees, makes any warranty, express or implied, or assumes any legal liability or responsibility for the accuracy, completeness, or usefulness of any information, apparatus, product, or process disclosed, or represents that its use would not infringe privately owned rights. Reference herein to any specific commercial product, process, or service by trade name, trademark, manufacturer, or otherwise does not necessarily constitute or imply its endorsement, recommendation, or favoring by the United States Government or any agency thereof. The views and opinions of authors expressed herein do not necessarily state or reflect those of the United States Government or any agency thereof.

Acknowledgments

The authors would like to acknowledge OLI Systems for providing access to their modeling software.

References

1. J. W. Carey, *Rev. Mineral. Geochemistry*, **77**, 505–539 (2013).

2. K. Agapiou and S. Charpiot, *Int. Cem. Rev.*, **August**, 113–116 (2013).

3. D. Brondel, R. Edwards, A. Hayman, D. Hill, and T. Semerad, *Oilf. Rev.*, 4–18 (1994).

4. A. Poursaee and C. M. Hansson, *Cem. Concr. Res.*, **37**, 1127–1133 (2007).

5. C. Andrade, P. Merino, X. R. Nóvoa, M. C. Pérez, and L. Soler, *Mater. Sci. Forum*, **192-194**, 891–898 (1995).

6. J. William Carey, R. Svec, R. Grigg, J. Zhang, and W. Crow, *Int. J. Greenh. Gas Control*, **4**, 272–282 (2010).

7. S. A. Carroll, W. W. McNab, and S. C. Torres, *Geochem. Trans.*, **12**, 9 (2011).

8. W. Um, H. Jung, S. Kabilan, C. A. Fernandez, and C. F. Brown, *Energy Procedia*, **63**, 5808–5812 (2014).

9. Y. Guo et al., *Int. J. Electrochem. Sci*, **8**, 12769–12779 (2013).

10. P. Lambert, C. L. Page, and P. R. W. Vassie, *Mater. Struct.*, **24**, 351–358 (1991).

11. G. Fierro, G. M. Ingo, and F. Mancia, *CORROSION*, **45**, 814–823 (1989).

12. T. Ramgopal, F. Gui, J. Hawk, and M. Ziomek-Moroz, NACE *CORROSION 2011*, Paper 11108, 1–11 (2011).

13. M. Ziomek-Moroz, *J. Mater. Eng. Perform.*, **21**, 1061–1069 (2012).

14. A. Sengupta, J. Beck, H. Zhao, R. Schatz, M. Ziomek-Moroz, S. N. Lvov, *ECS Transactions*, **66**, p. 37-50 (2015).

15. International Standards Organization, American National Standards Institute, and NACE International, **ANSI/NACE** (2009).

16. R. Heidersbach, *Metallurgy and Corrosion Control in Oil and Gas Production*, p. 213-222, Wiley, Hoboken, N.J, (2011).

17. Y. S. Shvarov and E. N. Bastrakov, *Aust. Geol. Surv. Organ.*, **Record 199** (1999).

18. R. Robie, B. Hemingway, and J. Fisher, *US Geol. Surv.*, **1452** (1978).

19. I. Zaytzev, Ed., *Properties of Aqueous Solutions of Electrolytes.*, CRC Press, Inc., Boca Raton, (1992).

20. ASTM International, in *Annual Book of ASTM Standards*,, p. 1–9 (2010).

21. M. Stern, *CORROSION*, **14**, 60–64 (1958).

22. M. Stern and A. L. Geary, *J. Electrochem. Soc.*, **104**, 56–63 (1957).

23. R. Feng et al., *NACE CORROSION 2016*, **To be presented** (2016).

24. D. Landolt, *Corrosion and Surface Chemistry of Metals*, p. 312-329, EPFL Press, (2007).